232 (2024) 212439

Contents lists available at ScienceDirect

Geoenergy Science and Engineering

journal homepage: www.sciencedirect.com/journal/geoenergy-science-and-engineering

Contribution of lamellation fractures to porosity and permeability of shales: A case study of the Jiaoshiba area in the Sichuan Basin, China

Lianbo Zeng [a,b,c,*], Xiang Xu [d,b,**], Shijie Ma [a,b], Hanyong Bao [e], He Tian [a,b], Zhe Mao [a,b], Mehdi Ostadhassan [f], Shaoqun Dong [a,b], Wenya Lyu [a,b]

[a] State Key Laboratory of Petroleum Resources and Prospecting, China University of Petroleum (Beijing), Beijing, 102249, China
[b] College of Geosciences, China University of Petroleum, Beijing, 102249, China
[c] Institute of Energy, Peking University, Beijing 100871, China
[d] Hunan Earthquake Agency, Changsha, 410004, China
[e] Research Institute of Exploration and Development, Jianghan Oilfield Company, SINOPEC, Wuhan 430223, China
[f] Department of Earth Science, Northeast Petroleum University, Daqing 163318, China

ARTICLE INFO

Keywords:
Lamellation fracture
Porosity
Permeability
Marine shale gas
Sichuan basin

ABSTRACT

Lamellation fractures are an important type of natural fracture in marine shales. These fractures affect the hydraulic connectivity of shale reservoir, however, their contribution to porosity and permeability is poorly understood. In this paper, we investigate the contribution of lamellation fractures to porosity and permeability of shale reservoirs in the Wufeng-Longmaxi Formation in Sichuan Basin. To do so, several analytical methods including scanning electron microscopy (SEM), CO_2 and N_2 adsorption experiments, high-pressure mercury injection (MICP), and permeability measurements under different confining pressures were combined. Results showed that the contribution of micro-pores, meso-pores, macro-pores, and fractures to pore volume is 29.1%, 35.7%, 12.6%, and 22.6%, respectively lamellation fractures can increase porosity 6%–10%. Besides, filling materials of the lamellation fractures, anhydrite, pyrite, and organic matter (OM), can improve shale petrophysical properties. Furthermore, it was found that lithofacies would cause different pressure sensitivities in permeability with clay rich shale being the highest and silty shale the lowest. In addition, samples with lamellation fractures exhibited higher pressure sensitivity while permeability steadily decreases with confining pressure, with its decreasing rate gradually slowing down in separate phases. Ultimately, lamellation fractures can increase horizontal permeability three at 5 MPa and two at 50 MPa of confining pressure. When compared to the actual formation pressure at 30 MPa, the permeability of shale samples with lamellation fractures is much higher than that without lamellation fractures. This study provides direct evidence that subsurface lamellation fractures can improve the storage space and permeability of shale reservoirs.

1. Introduction

In the past decade, there is a great success in the exploration and development of shale plays around the world (Curtis, 2002; Gale et al., 2007; Selley, 2012). The commercial production of Shale gas in Jiaoshiba area ranks first in China (Guo, 2019; Shi et al., 2020; Wang et al., 2020). Gas production from this play reached more than 2.0 × 10^{11} m^3 at the end of 2018 (Gou et al., 2019), making it the second largest shale gas field globally, excluding the North American plays (Yi et al., 2019).

Lamellation fractures are defined as cracks parallel or sub-parallel to the direction of the lamellation, which is widely developed in marine shale and contributes to porosity and permeability to a large extent (Zeng et al., 2016, 2021; Wang et al., 2017; Xu et al., 2021; Chen et al., 2021). Lamellation fractures always are considered as main fluid flow conduits and can enhance appropriate porosity, which ultimately affect the accumulation and production of shale gas (Hill and Nelson, 2000; Comer, 2008; Kassis and Sondergeld, 2010; Tian et al., 2021). Lamellation fractures are usually visible on the core and can be detected by logging data (Lai et al., 2022; Pang et al., 2023). The origin of

* Corresponding author. State Key Laboratory of Petroleum Resources and Prospecting, China University of Petroleum (Beijing), Beijing, 102249, China.
** Corresponding author.Hunan Earthquake Agency, Changsha, 410004, China.
E-mail addresses: xuxiangdike@163.com (L. Zeng), lbzeng@sina.com (X. Xu).

https://doi.org/10.1016/j.geoen.2023.212439
Received 17 May 2023; Received in revised form 21 September 2023; Accepted 23 October 2023
Available online 2 November 2023

lamellation fracture is triggered by fluid overpressure related to hydrocarbon generation in organic-rich shale (Cobbold et al., 2013; Xu et al., 2021). In addition, the occurrence of acid fluids in the hydrocarbon generation stage can dissolve some minerals to change the sensitivity of the shales (Zeng et al., 2013), which is more conducive to forming lamellation fractures.

It is well known that shale is a type of unit with dual porosity and fracture. In addition to changing permeability properties, fractures also provide appropriate porosity. The pore-fracture network is a collective name for various types of void spaces (Chalmers and Bustin, 2007; Clarkson et al., 2013; Wang et al., 2019) and is divided into micro-pores (pore diameter <2 nm), meso-pores (pore diameter 2–50 nm), macro-pores (pore diameter 50 nm–2 μm), and micro-fractures (pore diameter >2 μm) (IUPAC, 1994; Gou et al., 2019). To assess the complex pore-fracture structure of shale, various techniques have been combined to quantitatively characterize the space structure (Loucks and Ruppel, 2007; Tian et al., 2013; Klaver et al., 2015; Wang et al., 2016; Zhang et al., 2018; Ju et al., 2018) such as CO_2 adsorption, N_2 adsorption, and high-pressure mercury intrusion, corresponding to micro-pores, meso--pores, and macro-pores or fractures (Ross and Bustin, 2007). The synthetical methods have been widely used to evaluate pore-fracture size distribution in shale plays including Haynesville, Woodford, Barnett, Bakken, Marcellus, and Jiaoshiba shales (Chalmers et al., 2012; Clarkson et al., 2013; Mastalerz et al., 2013; Wang et al., 2020). Although the widespread use, previous studies seem to focus more on the contribution of pores, but less consideration is given to the contribution proportion of lamellation fractures. In other words, the unique contribution to porosity due to the lamellation fractures has been neglected, because lamellation fractures are not separated from micro-fractures.

Because the permeability of shale reservoirs ranges from nanometers to micrometers, one key feature to boost permeability would be lamellation fractures that occur parallel to the bedding that are a unique geologic feature of shales (Morgan and Einstein, 2017). Hence, permeability anisotropy, fracture mechanics and related failure strength of shale can be attributed primarily to these bedding fracturing (Kwon et al., 2001, 2004; Louis et al., 2009; Morgan and Einstein, 2017). For example, the permeability measured perpendicular to the bedding is three to four times lower than that measured parallel to the bedding (Gentzis et al., 2007). Therefore, more attention should be paid to the lamellation fractures and we should consider the effect of both lamellation fractures and other natural fractures when quantifying the permeability of shale.

Moreover, the permeability of shale reservoirs is sensitive to stress, and with the increase of effective stress, the permeability of the reservoir decreases (McKee et al., 1988; Kwon et al., 2001; Dong et al., 2010; Kassis and Sondergeld, 2010). This means production from the reservoirs will cause the pore pressure to decrease and an increase in effective stress and fracture closure (Davudov and Moghanloo, 2018). This would result in permeability changes in several magnitudes, thus further affecting horizontal hydraulic connectivity ultimately (Bustin et al., 2008; Ross and Bustin, 2008; Dong et al., 2010). Therefore, it is necessary to measure the permeability of shale reservoirs versus pressure, especially the fracture aperture status (being open or closed) to better understand their contribution to the flow.

In this study, the pore-fracture size distribution of marine shales was investigated in the Wufeng-Longmaxi Formation by carbon dioxide (CO_2), nitrogen (N_2) gas adsorption analyses and high-pressure mercury intrusion porosimetry (MIP) experiments, and calculated the volume proportion of lamellation fractures in total porosity. We also conducted flow experiments under different confining pressures to discuss the pressure sensitivity of permeability and the contribution of l lamellation fractures to permeability variations. Finally, we specially evaluated the effect of lamellation fracture on the permeability and fluid flow in shale gas reservoirs.

2. Geological settings

The Jiaoshiba Area is located in the eastern Sichuan Fold Belt in the boudraies of Sichuan Basin (Fig. 1). It is bounded by the Huaying Mountain Faul in the west, and the Qiyue Mountain Fault at the edge of the basin in the east (Guo and Zhang, 2014; Hu et al., 2014). The boundary of the research area is controlled by Diaoshuiyan Fault and Shimen Fault in the NE-SW direction, and Daershan and Wujiang Faults in the NW-SE direction (Gou and Xu, 2019), appearing a slightly deformed box shaped anticline in the NE-SW direction, with underdeveloped faults (Ma et al., 2007; Hao et al., 2013).

The Jiaoshiba Area has undergone multiple-phase tectonic evolution with the strata ranging from Late Sinian to the Late Cretaceous period (Zhao et al., 2016; Wang et al., 2018). During the Wufeng-Longmaxi Formation deposition period, shales were deposited between deep and shallow shelves in a reduction environment (Zhang et al., 2020). According to the mineral composition, the shales from the bottom to the top were divided into nine layers while the target stratum is characterized by obvious trichotomy. As shown in Fig. 2, Layers 1–5 are composed of black siliceous shale, containing abundant siliceous biological fossils. Layers 6–7 are mainly are mainly composed of gray-black silty shale. Note that the siliceous components here are mainly terrestrial silts with rare biological fossils. Layers 8–9 are mainly composed of gray and dark gray clay shale, with low siliceous content (Tuo et al., 2016; Guo, 2019).

3. Materials and methods

3.1. Shale samples

In this study, 34 core samples from well JY-A in the Jiaoshiba Area were selected for electron microscopy, while six are mechanically polished and 28 are argon-ion polished. Furthermore, six additional samples (JY-1 to JY-6) that are drilled parallel to the bedding plane were chosen for N_2 adsorption, CO_2 adsorption, and MICP (Fig. 3 and Table 1). These samples were also measured for permeability variations under different confining pressures. In addition, a vertical sample (JY-7) at the same depth of JY-6 sample was used as a control sample for permeability measurements. Based on general core observations, samples JY-1 to JY-3 are siliceous shale, JY-4 is silty shale, and JY-5 to JY-7 are shale rich in clay minerals. We should clarify that samples JY-1 to JY-5 are drilled in the shale with lamellation fractures. All detailed information about these samples and the experiments they were exposed to are listed in Tables 1 and 2.

3.2. Scanning electron microscopy

There are 34 samples that were cut and polished and coated with a layer of gold. Among them, 6 samples were polished mechanically, and 28 samples were argon ion milled. Sample preparation and imaging was done in the China University of Petroleum (Beijing). The SEM analysis was carried out using a Quanta 200 F SEM with a maximum resolution of 10 nm.

3.3. High-pressure mercury injection experiments (MICP)

The Pore master automatic mercury porosimeter was used for MICP measurement, following the SY/T5346-2005 standard. The experiment was completed at the Institute of Percolation Mechanics of Research Institute of Petroleum Exploration and Development, China. Before the experiment, the samples were dried to a constant weight at 105 °C. Mercury will enter pores as pressure increases with an operating pressure up to 30,000 psi, and Washburn equation can be used to obtain the relationship between pore diameter and the external pressure (Washburn, 1921), based on the assumption that all pores are cylindrical in shape.

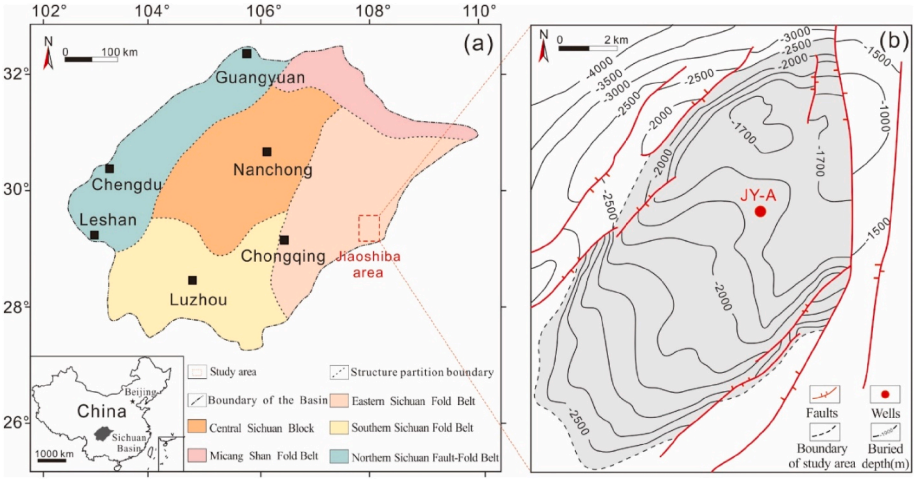

Fig. 1. (a) Location of the study area (the dotted rectangle) and tectonic division of the Sichuan Basin. (b) Structural features in the Jiaoshiba Area. The red dot is the location of the well where samples are retrieved.

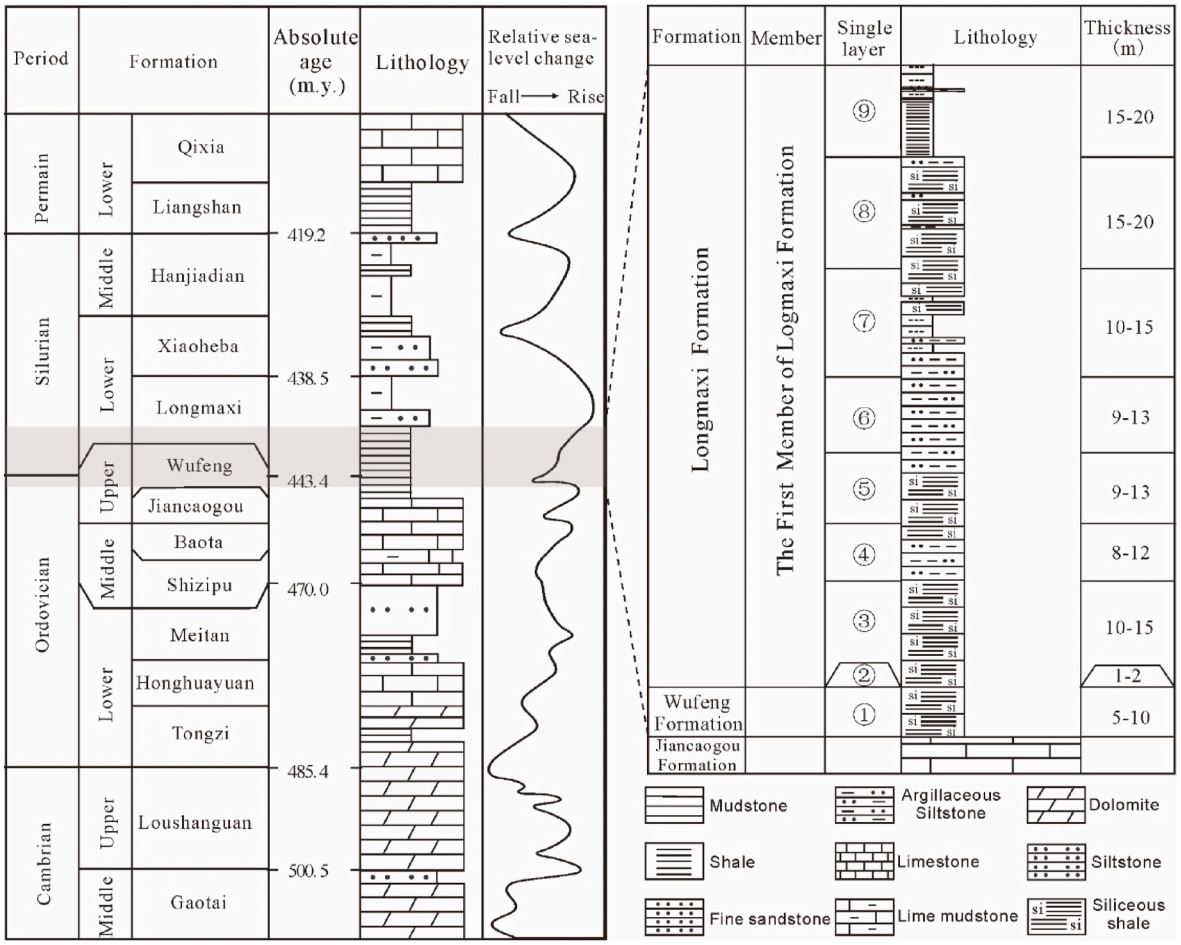

Fig. 2. The stratigraphic column in the Jiaoshiba Area. Note that the enlarged part marked gray represents the targeted strata in this study (modified from Xu et al., 2021).

3.4. Gas adsorption experiments in low temperature

The instrument used was an Autosorb-6B pore size analyzer. Before the experiments, the samples were crushed and sieved with 60–80 mesh, dried, and desorbed in a vacuum environment for 24 h to remove moisture. The temperature of the nitrogen adsorption experiment is 77.35 K, and the relative pressure ranges from 0.005 to 1.0. The temperature of carbon dioxide experiments is 273.15 K, with the relative pressure ranging from 0.0005 to 0.029. Then, the pore diameter and pore volume can be calculated by combining the Barrett Joyner Halenda (BJH) model and the density functional theory (DFT) model (Clarkson et al., 2013).

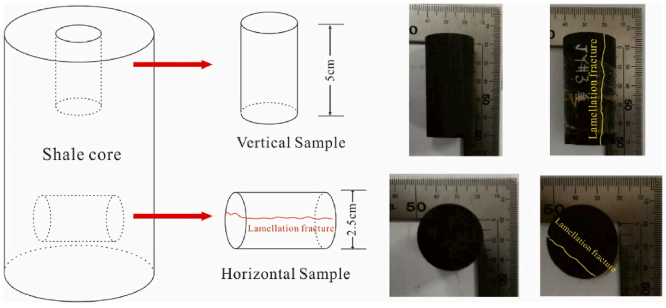

Fig. 3. Schematic diagram of Wufeng-Longmaxi Formation shale sample in well JY-A in the Jiaoshiba Area, including vertical and horizontal sampling.

3.5. Permeability tests under different confining pressures

The equipment that was used is the permeability testing system developed and assembled in house by the Institute of Percolation Mechanics of Research Institute of Petroleum Exploration and Development, China, as shown in Fig. 4. Nitrogen with a purity of 99.99% was used for permeability measurements. The sample is placed in the core holder and was injected with constant pressure of while confining pressures were increased in the following order: 5, 10, 15, 20, 30, 40, and 50 (MPa). Finally, the gas flow rate at the outlet corresponding to different confining pressures is measured at atmospheric pressure.

4. Results

4.1. Results of SEM experiments

According to the pore classification proposed by Loucks et al. (2012), four types of pore spaces were observed in the study area. The organic matter pores (OM-P) is the intragranular residual void formed in the hydrocarbon generation process of organic matter. Generally, organic matter can be divided into situ organic matter and migration organic matter (Chalmers et al., 2012). The in-situ organic matters are usually kerogen, and the organic pores that are developed would have a better continuity while such pores are often relatively flat due to kerogen's weak anti-compression ability (Fig. 5a). Migration organic matter refers to the organic matter that once migrated over a short distance. They are usually distributed in the primary intergranular pores of the reservoirs. The organic matter pores formed in this type of organic matter usually exhibit a perfectly circular and complete shape. This is because the brittle mineral particles bear the pressure of the overlying strata (Fig. 5b). SEM images show that graptolite fragments lack any pore spaces while some inter-particle pores (Inter-P) and micro-fractures (MF) often develop at the boundary between the graptolite fragments and other minerals (Fig. 5c). Following compaction, cementation, and dissolution, some inter-particle pores and micro-fractures will form at the edges of brittle minerals (Fig. 5d). The scale of micro-fractures is small and they lack lateral persistence (Fig. 5c and d), however, lamellation fractures tend to extend longer and distribute more regularly than micro-fractures. Intra-particle pores (Intra-P) can be formed due to dissolution, such as those pores in calcite particles (Fig. 5d) or because of crystals rearrangement, such as the intra-particle pores in pyrite (Fig. 5e). Lamellation fractures are distributed parallel or sub-parallel to the bedding (Fig. 5f). The fracture aperture can differ significantly, ranging from 1 μm to 1000 μm.

4.2. Results of high-pressure mercury injection experiments

The mercury intrusion curves of samples JY-1, JY-2, JY-3, JY-5, and JY-6 are similar and the curve can be divided into three sections, one up to 0.1 MPa, then up to 40 MPa and then beyond 40 MPa (Fig. 6a). Fig. 6b demonstrates the cumulative pore volume showing a rapid rise when the pore size exceeds 2000 nm. This indicates that the pore volume of shale samples in the Jiaoshiba Area increases when the pore size reaches 2–50 μm. Moreover, the cumulative pore volume also increases notably in sample JY-4 in specificlly in the pore size range from 50 nm to 200 nm (Fig. 6b).

Table 2
Experiments conducted on each sample with the goal of experiment.

Types of experiments	Sample number	Goal
Scanning electron microscopy	34 samples from well JY-A	Observe the types and feature of pore-fracture spaces
High-pressure mercury intrusion	6 samples from well JY-A (samples JY-1 to JY-6)	Obtain the size distribution of pores or fractures with a pore diameter greater than 50 nm.
N_2 adsorption	6 samples from well JY-A (samples JY-1 to JY-6)	Obtain the size distribution of pores with a pore diameter from 1.5 nm to 79 nm
CO_2 adsorption	6 samples from well JY-A (samples JY-1 to JY-6)	Obtain the size distribution of pores with a pore diameter from 0.3 nm to 1.5 nm.
Permeability test	7 samples from well JY-A (samples JY-1 to JY-7)	Obtain the permeability of the sample when the confining pressure changes from 5 MPa to 50 MPa

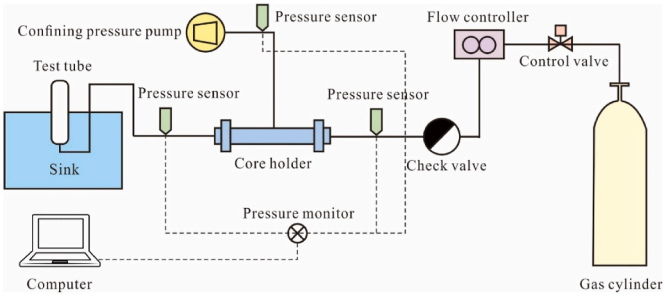

Fig. 4. Schematic diagram of the permeability experimental setup.

Table 1
Geological information of shale samples from the Wufeng-Longmaxi Formation in well JY-A in the Jiaoshiba Area.

Sample ID	Depth (m)	TOC (Wt %)	Mineral Content (Wt %)					Lithology	Layer	Direction	Lamellation Fractures
			Quartz	Clay	Feldspar	Carbonate	Pyrite				
JY-1	2327.6	2.13	42	37.3	8.6	6.5	5.6	Siliceous shale	5	Horizontal	Yes
JY-2	2335.8	2.47	37.6	37.3	8.3	12.2	4.6	Siliceous shale	4	Horizontal	Yes
JY-3	2352.2	3.24	59	21.1	7.3	8.9	3.7	Siliceous shale	3	Horizontal	Yes
JY-4	2318.3.	1.46	34.8	37.5	16	9.5	2.2	Silty shale	6	Horizontal	Yes
JY-5	2296.2	2.18	28.6	47.2	5.3	13	5.9	Clay shale	8	Horizontal	Yes
JY-6	2297.6	1.74	31.7	47.7	8	7.2	5.4	Clay shale	8	Horizontal	No
JY-7	2297.6	1.74	31.7	47.7	8	7.2	5.4	Clay shale	8	Vertical	No

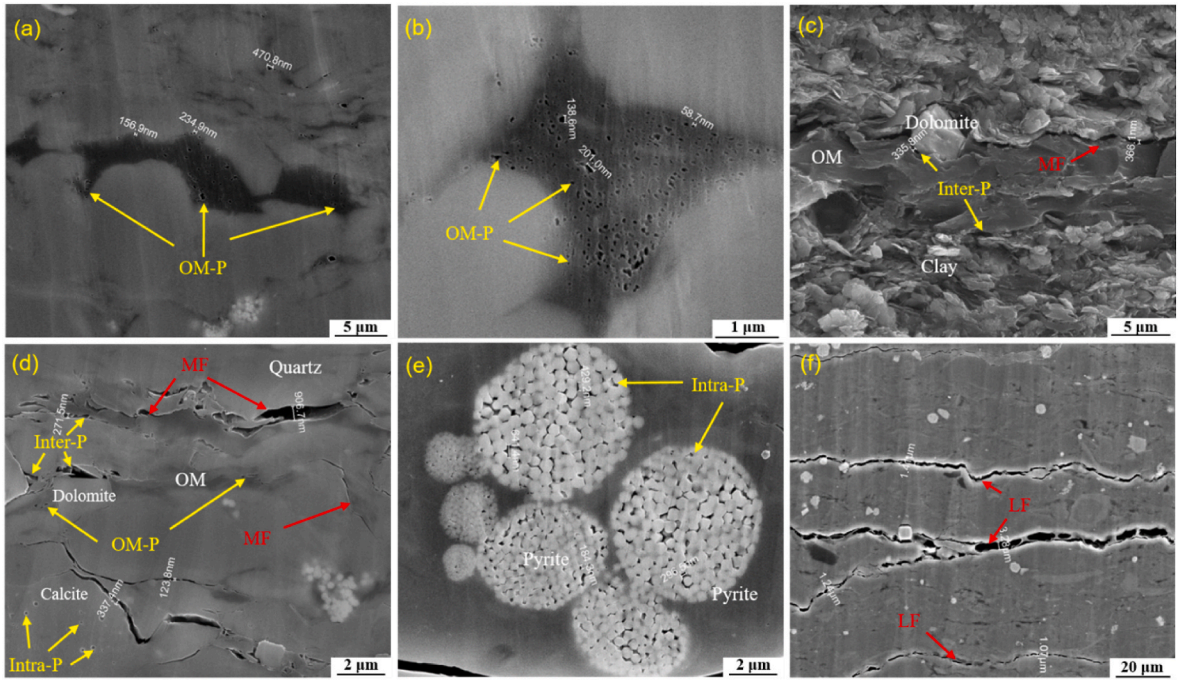

Fig. 5. Different exisiting pores identified in our samples. (a) OM pores in kerogen; (b) OM pores in migration organic matter; (c) Inter-particle pores and micro-fractures (MF) between graptolite fragments and other minerals; (d) Inter-particle pores between brittle minerals, intra-particle pores inside brittle minerals, and micro-fractures; (e) Intra-particle pores in pyrite; (f) Nearly parallel Lamellation fractures (LF).

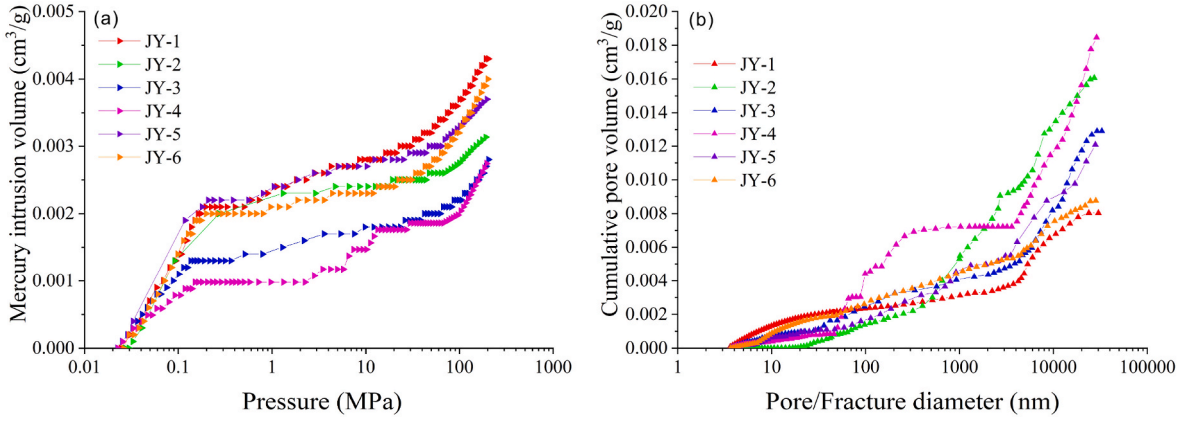

Fig. 6. (A) MICP curve of all six samples tested in this study; (b) Cumulative distribution of pore volume of shale samples that is obtained from saturation curves.

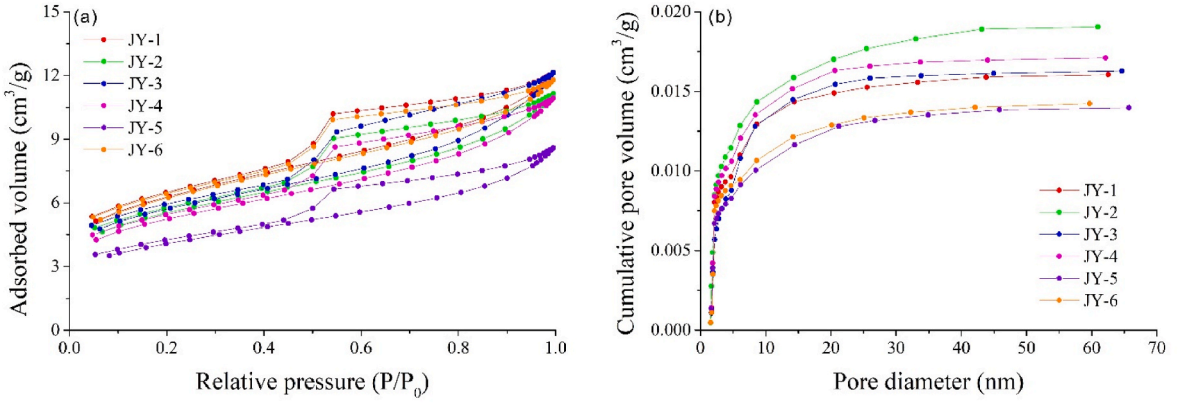

Fig. 7. (a) N_2 adsorption and desorption curve; (b) Cumulative distribution of pore volume under N_2 adsorption experiment.

4.3. Results of gas adsorption experiments in low temperature

Based on the morphology of N_2 adsorption and desorption curve, the ink-bottle and slit shaped pores are recognized in the samples (Fig. 7a). The cumulative pore volume curve shows the meso-pore pore diameter in this area is mainly below 10 nm, where the curve rises rapidly (Fig. 7b). The larger the pore size, the slower the rate of changes of the corresponding pore volume, thus the lower proportion.

CO_2 gas adsorption results show type I curve and the adsorption capacity of all six shale samples increases with increasing relative pressure. We'd like to recall that type I curves reflect multiple morphological micro-pore structures (Wang et al., 2018). Fig. 8b shows that most pores sizes are less than 0.7 nm and mainly distributed in the range of 0.3nm–0.7 nm. When pore size exceeds than 0.7 nm, pore volume gradually increases which means that there exist relatively fewer pores larger than 0.7 nm. However, within the pore size range of 0.3 nm–0.7 nm, the cumulative pore volume increases with a steeper slope, and we infer that the micro-pore volume mainly is resulting from pores smaller than 0.7 nm.

4.4. Results of permeability tests under different confining pressures

Flow tests of the samples demonstrate that overall permeability decreases with higher confining pressure. Additionally, since the sample was free of natural or lamellation fractures, its value can be regarded as the matrix permeability which is found at 4×10^{-4} mD when confining pressure has not been applied and 6×10^{-5} mD at the confining pressure of 50 MPa. Furthermore, permeability values of samples 1–6 that are cut parallel to the bedding plane, can be regarded as horizontal permeability, of which samples 1–5 with lamellation fractures and samples 6 without lamellation fractures. Results show that permeability of sample 6 is 0.025 mD without any confining pressure and 0.003 mD under confining pressure of 50 MPa. Note that permeability of the five other samples with lamellation fractures is notably higher than sample 6. It can reach 1.5–17 mD under zero confining pressure and 0.1–1.3 mD under 50 MPa of confining pressure (Fig. 9a). Fig. 9b shows the rate or percentage of permeability reduction with confining pressure. Its seen from this figure that in the pressure range from 5 MPa to 20 MPa, the permeability decreases rapidly, and then it becomes slower. Overall, comparing all 7 shale samples we measured 78.1–98.8% of reduction in permeability when the pressure reaches 50 MPa. Comparing samples JY-6 and JY-7 particularly, it was understood that horizontal permeability of shale is much larger than the vertical permeability which has been reported by other studies (Kwon et al., 2004; Ma et al., 2016; Zhang et al., 2019). The ratio of horizontal to vertical permeability between these two samples is about 64.

5. Discussions

5.1. Contribution of lamellation fractures to porosity

The shale unit is a dual medium of fracture and pore. Besides pores, there are micro fractures in shale gas storage space. Shale gas shows two occurrence states, the sites of adsorbed gas are mainly micropores, while the sites of free gas are mainly macropores and microfractures. Therefore, the porosity provided by lamellation fractures may not be ignored in underground rock with lamellation fractures. Through CO_2 and N_2 adsorption, along with MICP measurements, various aspects of pore and fracture size distribution can be revealed. CO_2 adsorption mainly characterizes micro-pores, while N_2 adsorption illustrates meso-pores and high-pressure mercury intrusion macro-pores and fractures. Therefore, we can obtain an entire spectrum of pore-fracture volume distribution characteristics in the Wufeng-Longmaxi Formations. Additionally, based on the results, we can quantitatively evaluate the contribution of various pore and fractures to the porosity of the shale reservoirs in full details. To do so, Table 3 and Fig. 10 are created which is the comparison of different pore size groups (micro, meso, macro, and fracture) among all samples. Based on Fig. 10, three major peaks in different pore ranges, smaller than 1.5 nm, 2–10 nm, and 5–20 μm, can be found respectively. Their corresponding pore types are organic pores in kerogen or organic pores and fractures in migration of organic matters from scanning electron microscopy. Micro-pores and meso-pores are the two most abundant pore types among the six samples with the average pore volume proportion of 29.1% and 35.7% respectively. The average ratio of larger pores (macropores) reaches 12.6%, and the fracture volume is about 22.6% (Table 3). As observed in electron microscopy, most fractures belong to microfractures or lamellation fractures. Since, we did not observe any lamellation fractures in sample JY-6, the entire fracture volume for this sample which accounts for 17.21%, are microfractures. Considering samples JY-1 to JY-5, both lamellation fractures and microfractures are abundant with the fracture volume responsible for about 23.29%–27.23% of the entire pore volume which is significantly higher than sample JY-6. We believe, this major difference mostly results from lamellation fractures rather than microfractures. Therefore, the lamellation fractures can account for 6%–10% of shale pore volume, and can provide effective storage for shale gas.

The fracture volume that is obtained through high-pressure mercury injection experiments generally refers to the volume of the unfilled fractures, however, the contribution of mineralized lamellation fractures is also worth studying. Through SEM analysis, it is found that the fillings in the lamellation fractures are mainly anhydrite, pyrite, and asphalt (Fig. 11a, c, e). Anhydrite fillings are easily modified by acidic fluids, forming some secondary dissolution pores at the edges (Fig. 11b). Besides, it'd be easy for shrinkage fractures to form inside the anhydrite due to inner shrinking (Cao et al., 2020). All these secondary pores can

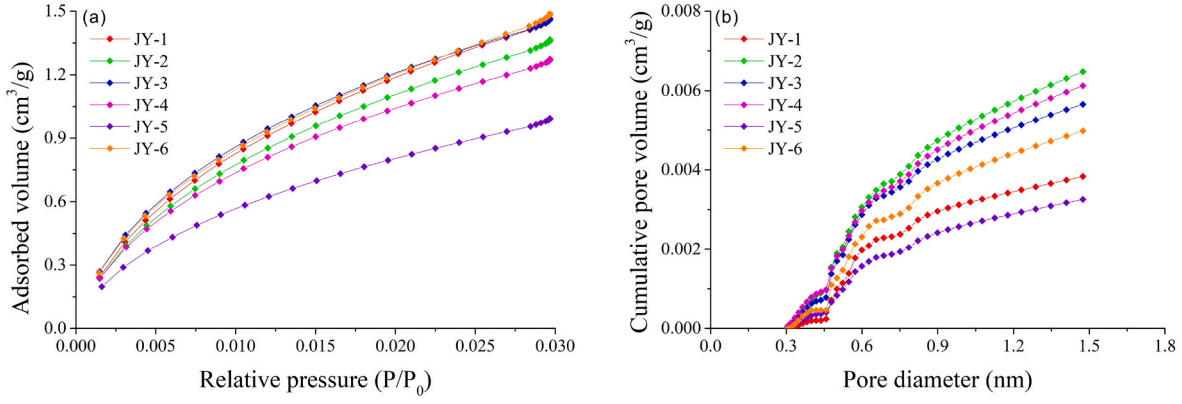

Fig. 8. (a) CO_2 adsorption curve of six shale sample; (b) Cumulative pore volume of shale samples under CO_2 adsorption experiment vs. pore diameter.

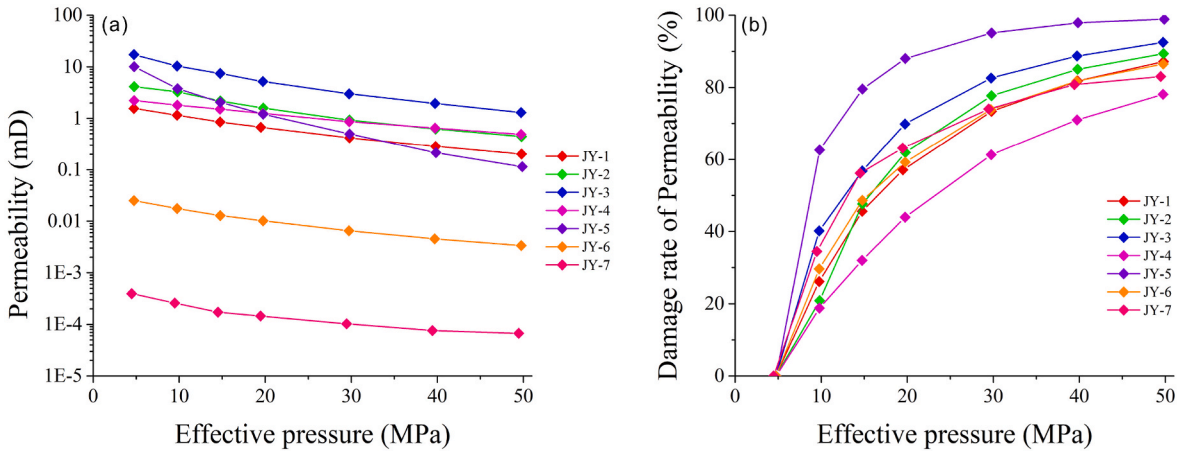

Fig. 9. (a) Permeability curves under different confining pressures; (b) The rate of permeability decrease under different confining pressures.

Table 3
The volume percentage of different pore types in the Wufeng-Longmaxi Formation in the Jiaoshiba Area.

Sample ID	Pore/Fracture volume (cm^3/g)				Volume percentage (%)			
	Micropores	Mesopores	Macropores	Fractures	Micropores	Mesopores	Macropores	Fractures
JY-1	0.0074	0.0089	0.0008	0.0052	33.09	39.81	3.81	23.29
JY-2	0.0112	0.0155	0.0041	0.0109	26.91	37.14	9.89	26.06
JY-3	0.0093	0.0124	0.0024	0.0090	26.46	37.45	7.26	27.23
JY-4	0.0103	0.0138	0.0063	0.0113	24.72	33.13	15.06	27.09
JY-5	0.0072	0.0109	0.0034	0.0075	24.72	37.42	11.73	26.13
JY-6	0.0085	0.0099	0.0025	0.0044	33.57	39.47	9.75	17.21

increase the storage space and improve the physical properties of the shale reservoirs. Lamellation fractures can also be filled with pyrite. These pyrite crystals are generally euhedral with uniform crystal grains. There are many intra-particle pores among the pyrite crystals (Figs. 11d and 5e), which are important storage spaces in shales. In addition, some migrating organic matter, such as asphalt, will fill the lamellation fractures. Such type of organic matters often experience substantial volume expansion during the hydrocarbon generation process, and lamellation fractures provide the space for the volume increase. When the volume expansion rate exceeds volume loss caused by fluid discharge and migration of produced hydrocarbons, formation over-pressure may occur (Li et al., 2016; Gao et al., 2019). The overpressure can helps the lamellation fractures to remain and organic pores to develop, leading to the retention of abundant organic pores of large size in the asphalt (Fig. 11f). In summary, the filled lamellation fractures can also improve the porosity due to the primary or secondary pores in the shale reservoirs.

5.2. Contribution of lamellation fractures to permeability

(1) Pressure sensitivity of the shales

The horizontal lamellation is highly present in shales leading to the anisotropy of shales (Xu et al., 2021). David et al. (1994) established an exponential model for the relationship between effective pressure and permeability:

$$K = K_0 \exp[-\gamma (P_e - P_0)] \quad (1)$$

Where K is the permeability at the effective pressure P_e, and K_0 is the permeability at the atmospheric pressure P_0, which is 0.1 MPa and γ is the pressure sensitivity coefficient. Larger γ values correspond to a more obvious permeability changes with effective pressure. Shi and Wang (1986) pointed out that the relationship between effective pressure and permeability should follow a power function:

$$K = K_0 (P_e / P_0)^{-p} \quad (2)$$

Where p is the material constant and larger p infers to easier the permeability changes with pressure and higher sensitivity of shale samples.

By fitting a curve to permeability values vs. pressure (Fig. 12), all required parameters based on these equations above can be obtained (Table 4). Except for lithology, samples JY-1 to JY-5, are similar in their preparation and distribution characteristics of lamellation fractures. Hence, this difference in lithology will cause a difference in pressure sensitivity values. In general, based on Table 4, the clayey shale samples have shown higher sensitivity coefficients of both γ (0.095) and p (1.93) that are much higher than siliceous shale samples with the average values of γ and p being 0.051 and 0.994, respectively. Silty shale samples were found with the lowest pressure sensitivity, with γ and p 0.034 and 0.652, respectively. We infer this to them being more resistant to pressure with more rigid mineral particles, and the pressure sensitivity to be lower in turn. Note that samples JY-6 and JY-7 come from different directions of the same core. Considering sample JY-6, parallel to the lamellation, the pressure sensitivity was found higher with γ and p as 0.044 and 0.862, respectively. This reflects that the horizontal permeability of shale samples (parallel to the lamellation) would have higher pressure sensitivity than vertical permeability (perpendicular to the lamellation). It's expected that the confining pressure increases, the lamellar clay minerals distributed along the bedding are compressed, and some microfractures along with the bedding also tend to close. All of these will cause significant changes in the permeability along the bedding direction. Samples JY-5 and JY-6 are different with the former containing lamellation fractures and thus more pressure sensitive, unlike the latter one. Shale, as a tight rock, has relatively low matrix permeability, so, the lamellation fractures contribute a lot to the permeability as the main fluid pathways. This also reflects the strong dependency on shale permeability on lamellation fractures and their aperture especially. It concluded that the lamellation fractures gradually

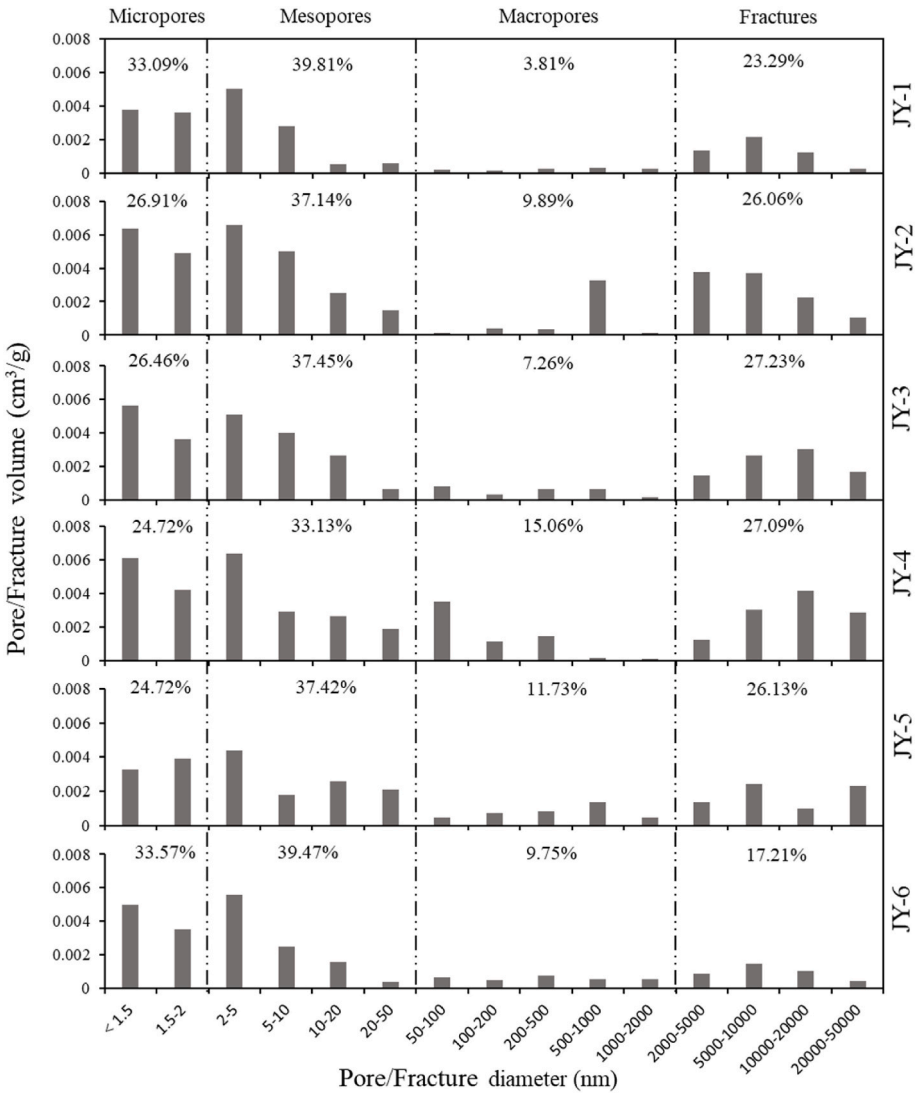

Fig. 10. Pore volume of different pore size intervals and groups of shale samples of the Wufeng-Longmaxi Formation in the Jiaoshiba Area.

will close as the pressure increases, resulting in the shale permeability decreasing rapidly.

The formation pressure of the Wufeng-Longmaxi Formation in the study area is about 30 MPa. The maximum confining pressure in this experiment has reached 50 MPa, which is appropriate to characterize underground pressure conditions in this area, in particular, lamellation fractures may have a significant impact on horizontal permeability. By comparing the samples JY-5 and JY-6 (Fig. 13), it is found that the permeability of the samples with lamellation fractures at 5 MPa is three orders of magnitude of the samples without lamellation fractures. Because other general geological parameters of these two samples are almost the same, and the sampling depth differs by 0.6 m, the such discrepancy in permeability can result from the lamellation fractures. When the confining pressure reaches 30 MPa, permeability decreases by 95.1% (Fig. 13) to 0.497 mD, which is still much larger than the permeability of the sample without lamellation fractures (sample JY-6). This indicates that lamellation fractures can significantly improve the permeability of shale reservoirs. At 50 MPa, the permeability of the samples with lamellation fractures is still two orders of magnitude of samples without lamellation fractures. In general, lamellation fractures can be used as flow conduits and can affect the migration of subsurface shale gas. The flow in shale is considered to follow a dual or triple porosity reservoir model with fractures to be the main flow pathways (Zhang et al., 2019), which is consistent with the results we found here.

The permeability of shale reservoirs gradually decreases with the increase of effective pressure, but the decreasing rate gradually slows down. Fig. 14 shows the rate of decrease can be divided into three parts relevant to the variation of the pressure: Phase A, Phase B, and Phase C. The corresponding effective pressure ranges are 5–20 MPa, 20–40 MPa, and 40–50 MPa for Phases A, B, and C, respectively (Fig. 14). Phase A is characterized by the rapid decline in the permeability phase. In this stage, the aperture of the lamellation fractures decreases because fracture walls come into contact with each other (Fig. 15). Phase B is the gradually decreasing rate in permeability where the aperture of the lamellation fractures is much smaller than before the pressure being applied. At this stage, the mechanical compaction of mineral particles, along with the reduction of inter-particle pore volume, and the closure of microfractures that can occur simultaneously causes a slow rate of permeability reduction. During Phase C, the permeability stays constant and its value barely decreases. In this stage, the compressible space in the fracture space has almost disappeared and mechanical compaction of such tight reservoirs cannot exceed a certain threshold to cause the permeability to reduce further.

6. Conclusions

(1) This study obtained the storage and pore structure in shale reservoirs with a variety of methods. Here we used quantitative

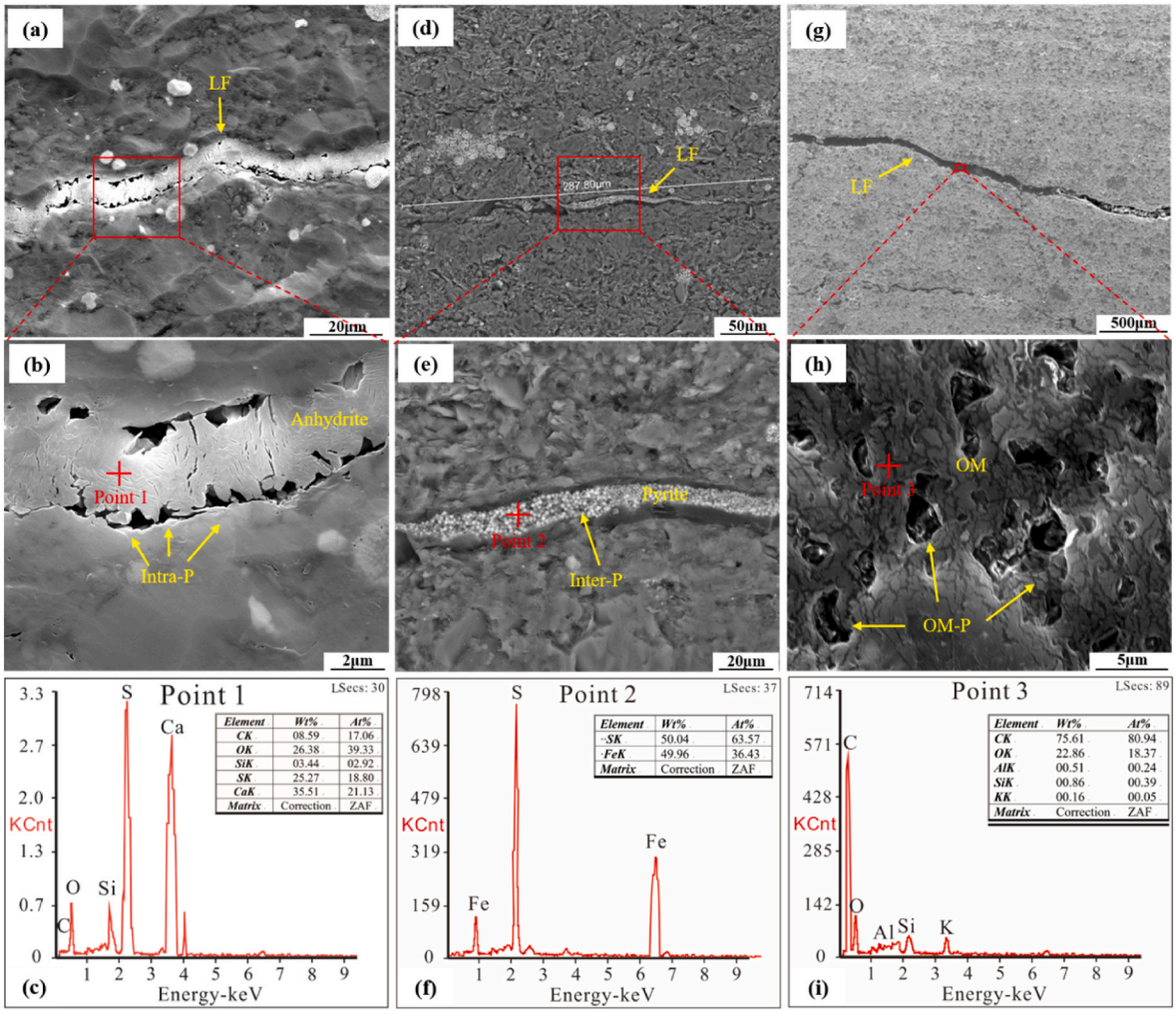

Fig. 11. (a) Anhydrite filling in the lamellation fractures; (b) dissolution pores that are developed on the edge of anhydrite, and shrinkage cracks inside; (c) energy spectrum of Point 1 in (b), that confirms the presence of anhydrite filling; (d) organic matter, and pyrite filling in the lamellation fractures; (e) A large number of inter-pores are developed inside the pyrite crystals; (f) the energy spectrum of Point 2 in (e), confriming the presenc of pyrite; (g) organic matter bitumen that has filled in the lamellation fractures; (h) A large number of organic pores formed inside organic matter; (i) the energy spectrum of point 3 in (h), which shows the abundance of carbon that would represent organic matter bitumen.

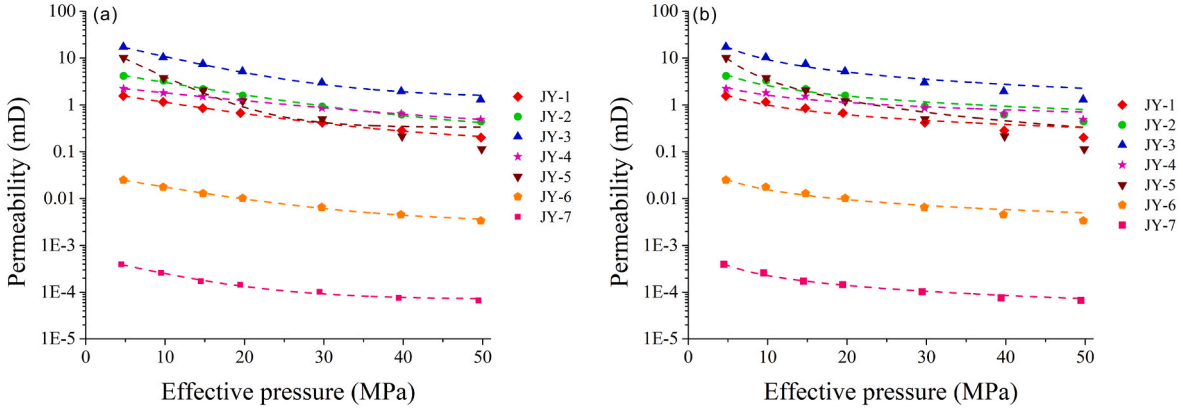

Fig. 12. (a) The fitted curve of the permeability data of shale samples based on the exponential equation of David et al. (1994); **(b) the fitted curve of the permeability of shale samples through the power law of** Shi and Wang (1986).

characterization of various pores-fracture volume percentages by N_2 and CO_2 absorption and MICP. Lamellation fractures can increase pore volume by 6%–10%, acting as an important storage space for shale reservoirs.

(2) Some lamellation fractures are filled with anhydrite, pyrite, and organic matter that can contribute to the pore volume. The dissolution pores and shrinkage fractures in anhydrite, the intercrystalline pores in the pyrite, and organic pores in organic

Table 4
Pressure sensitivity parameters from the Wufeng-Longmaxi Formation based on two different equations.

(2) The effects of lamellation fractures on permeability

Sample ID	Exponential relationship $K=K_0\exp[-\gamma(P_e-P_0)]$		Power law $K=K_0(P_e/P_0)^{-P}$		Lithology	Direction	Lamellation Fractures
	$\gamma(MPa^{-1})$	R^2	p	R^2			
JY-1	0.045	0.989	0.881	0.949	Siliceous shale	Horizontal	Yes
JY-2	0.051	0.982	0.996	0.946	Siliceous shale	Horizontal	Yes
JY-3	0.056	0.978	1.104	0.968	Siliceous shale	Horizontal	Yes
JY-4	0.034	0.995	0.652	0.931	Silty shale	Horizontal	Yes
JY-5	0.095	0.973	1.903	0.974	Clay shale	Horizontal	Yes
JY-6	0.044	0.981	0.862	0.964	Clay shale	Horizontal	No
JY-7	0.038	0.923	0.763	0.992	Clay shale	Vertical	No

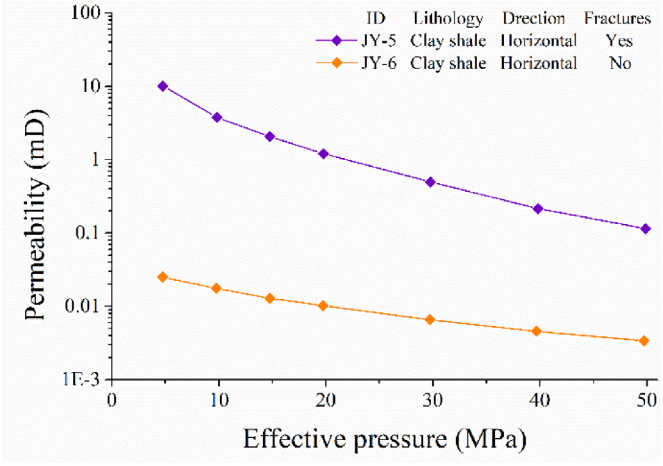

Fig. 13. The relationship between permeability and effective pressure of shale samples with and without lamellation fractures.

(3) Phases of permeability variations with pressure

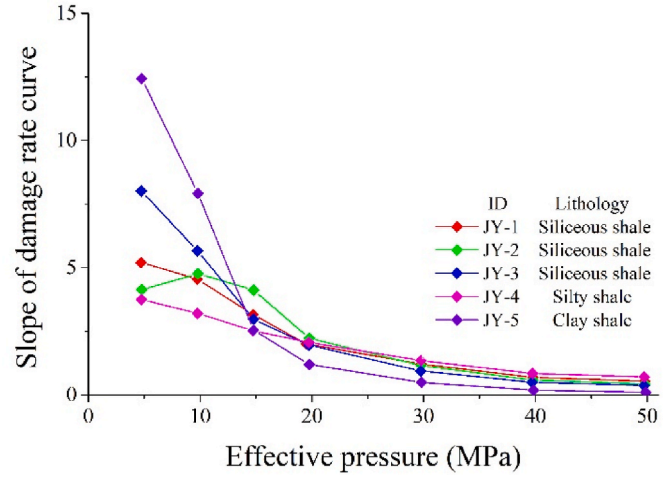

Fig. 14. Rate of permeability reduction with confining pressure of shale samples containing lamellation fractures.

matter increase the pore volume of shale reservoirs. The primary or secondary pores in these fillings can also be used as storage space for shale gas, which is conducive to shale gas enrichment.

(3) The horizontal permeability sensitivity of shale samples is higher than that of vertical direction. Additionally, lithofacies played a role in the pressure sensitivity of different samples. Clay-rich shale showed a higher pressure sensitivity than siliceous shale, while silty shale had the lowest pressure sensitivity. The presence of lamellation fractures will also impact pressure sensitivity where lamellation fractures increased horizontal permeability three times at 5 MPa and two times at 50 MPa.

(4) The permeability of shale gradually decreases with the increase of confining pressure, but its decline rate gradually slows down in three separate stages. The corresponding confining pressure ranges of such phases were found 5 MPa–20MPa, 20 MPa–40MPa, and 40 MPa–50MPa, respectively. Phase A marks the rapid permeability decline due to immediate fracture aperture closure followed by Phase B where reduction of inter-particle pores, and the closure of microfractures causes slower decrease of permeability in this period. Finally, in Phase C permeability stays almost constant due to the medium reaching its highest compaction threshold.

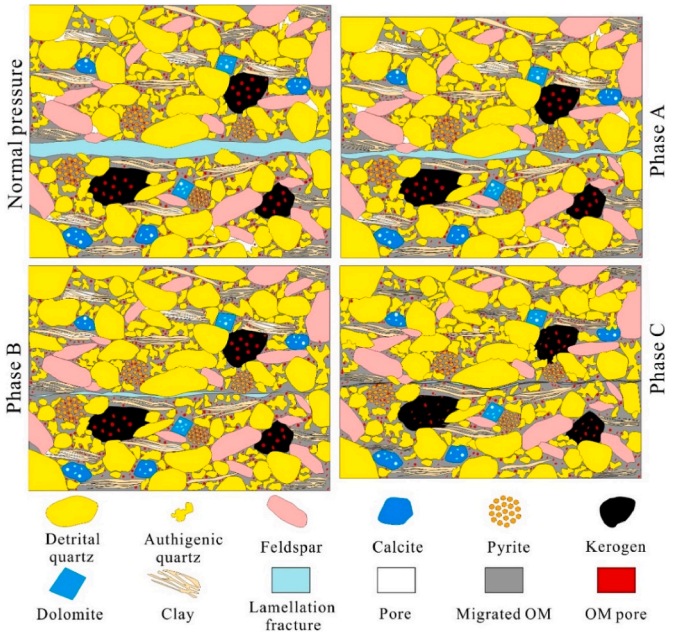

Fig. 15. Schematic diagram of the changes in the permeability of the lamellation fractures in each stage under overburden pressure.

Declaration of competing interest

The authors declare that they have no known competing financial interests or personal relationships that could have appeared to influence the work reported in this paper.

Data availability

The data that has been used is confidential.

Acknowledgments

The authors are very grateful for the shale samples provided by the Research Institute of Petroleum Exploration and Development of SINOPEC Jianghan Oilfield Company and the help provided by the Institute of Percolation Mechanics of Research Institute of China Petroleum Exploration and Development in the experiments. The financial support by the National Natural Science Foundation of China (Grant No. U1663203) is greatly appreciated.

References

Bustin, R.M., Bustin, A.M.M., Cui, X., Ross, D.J.K., Pathi, V.S.M., 2008. Impact of shale properties on pore structure and storage characteristics. In: Society of Petroleum Engineers - Shale Gas Production Conference 2008, pp. 32–59. https://doi.org/10.2118/119892-MS.

Cao, T., Xu, H., Liu, G., Deng, M., Cao, Q., Yu, Y., 2020. Factors influencing microstructure and porosity in shales of the Wufeng-Longmaxi formations in northwestern Guizhou, China. J. Petrol. Sci. Eng. 191 https://doi.org/10.1016/j.petrol.2020.107181.

Chalmers, G.R.L., Bustin, R.M., 2007. The organic matter distribution and methane capacity of the Lower Cretaceous strata of Northeastern British Columbia, Canada. Int. J. Coal Geol. 70, 223–239. https://doi.org/10.1016/j.coal.2006.05.001, 1–3 SPEC. ISS.

Chalmers, G.R.L., Bustin, R.M., Power, I.M., 2012. Characterization of gas shale pore systems by porosimetry, pycnometry, surface area, and field emission scanning electron microscopy/transmission electron microscopy image analyses: examples from the Barnett, Woodford, Haynesville, Marcellus, and Doig units. AAPG (Am. Assoc. Pet. Geol.) Bull. 96 (6), 1099–1119. https://doi.org/10.1306/10171111052.

Chen, Y., Jiang, C., Leung, J.Y., Wojtanowicz, A.K., Zhang, D., 2021. Multiscale characterization of shale pore-fracture system: geological controls on gas transport and pore size classification in shale reservoirs. J. Petrol. Sci. Eng. 202 https://doi.org/10.1016/j.petrol.2021.108442.

Clarkson, C.R., Solano, N., Bustin, R.M.M., Bustin, A.M.M., Chalmers, G.R.L., He, L., Melnichenko, Y.B., Radliński, A.P., Blach, T.P., 2013. Pore Structure Characterization of North American Shale Gas Reservoirs Using USANS/SANS, Gas Adsorption, and Mercury Intrusion, in Fuel, pp. 606–616. https://doi.org/10.1016/j.fuel.2012.06.119.

Cobbold, P.R., Zanella, A., Rodrigues, N., Løseth, H., 2013. Bedding-parallel fibrous veins (beef and cone-in-cone): worldwide occurrence and possible significance in terms of fluid overpressure, hydrocarbon generation and mineralization. Mar. Petrol. Geol. 43, 1–20. https://doi.org/10.1016/j.marpetgeo.2013.01.010.

Comer, J.B., 2008. Reservoir characteristics and production potential of the Woodford Shale. World Oil 229 (8), 83–89.

Curtis, J.B., 2002. Fractured shale-gas systems. AAPG (Am. Assoc. Pet. Geol.) Bull. 86 (11), 1921–1938.

David, C., Wong, T.F., Zhu, W., Zhang, J., 1994. Laboratory measurement of compaction-induced permeability change in porous rocks: implications for the generation and maintenance of pore pressure excess in the crust. Pure and Applied Geophysics PAGEOPH 143 (1–3), 425–456. https://doi.org/10.1007/BF00874337.

Davudov, D., Moghanloo, R.G., 2018. Impact of pore compressibility and connectivity loss on shale permeability. Int. J. Coal Geol. 187, 98–113. https://doi.org/10.1016/j.coal.2018.01.008.

Dong, J.J., Hsu, J.Y., Wu, W.J., Shimamoto, T., Hung, J.H., Yeh, E.C., Wu, Y.H., Sone, H., 2010. Stress-dependence of the permeability and porosity of sandstone and shale from TCDP Hole-A. Int. J. Rock Mech. Min. Sci. 47 (7), 1141–1157. https://doi.org/10.1016/j.ijrmms.2010.06.019.

Gale, J.F.W., Reed, R.M., Holder, J., 2007. Natural fractures in the Barnett Shale and their importance for hydraulic fracture treatments. AAPG (Am. Assoc. Pet. Geol.) Bull. 91 (4), 603–622. https://doi.org/10.1306/11010606061.

Gao, J., kun Zhang, J., He, S., xin Zhao, J., liang He, Z., jin Wo, Y., xing Feng, Y., Li, W., 2019. Overpressure generation and evolution in Lower Paleozoic gas shales of the Jiaoshiba region, China: implications for shale gas accumulation. Mar. Petrol. Geol. 102, 844–859. https://doi.org/10.1016/J.MARPETGEO.2019.01.032.

Gentzis, T., Deisman, N., Chalaturnyk, R.J., 2007. Geomechanical properties and permeability of coals from the Foothills and Mountain regions of western Canada. Int. J. Coal Geol. 69 (3), 153–164. https://doi.org/10.1016/j.coal.2006.02.007.

Gou, Q., et al., 2019. Full-scale pores and micro-fractures characterization using FE-SEM, gas adsorption, nano-CT and micro-CT: a case study of the Silurian Longmaxi Formation shale in the Fuling area, Sichuan Basin, China. Fuel 253, 167–179. https://doi.org/10.1016/j.fuel.2019.04.116.

Gou, Q., Xu, S., 2019. Quantitative evaluation of free gas and adsorbed gas content of wufeng-longmaxi shales in the jiaoshiba area, sichuan basin, China. Advances in Geo-Energy Research 3 (3), 258–267. https://doi.org/10.26804/AGER.2019.03.04.

Guo, T., Zhang, H., 2014. Formation and enrichment mode of Jiaoshiba shale gas field, Sichuan Basin. Petrol. Explor. Dev. 41 (1), 31–40. https://doi.org/10.1016/S1876-3804(14)60003-3.

Guo, X., 2019. Major factors controlling the shale gas accumulations in Wufeng-Longmaxi Formation of the pingqiao shale gas field in fuling area, Sichuan Basin, China. Journal of Natural Gas Geoscience 4 (3), 129–138. https://doi.org/10.1016/j.jnggs.2019.06.002.

Hao, F., Zou, H., Lu, Y., 2013. Mechanisms of shale gas storage: implications for shale gas exploration in China. AAPG (Am. Assoc. Pet. Geol.) Bull. 97 (8), 1325–1346. https://doi.org/10.1306/02141312091.

Hill, D.G., Nelson, C.R., 2000. Gas productive fractured shales: an overview and update. Gastips 6 (2), 4–13.

Hu, D., Zhang, H., Ni, K., Yu, G., 2014. Preservation conditions for marine shale gas at the southeastern margin of the Sichuan Basin and their controlling factors. Nat. Gas. Ind. B 1 (2), 178–184. https://doi.org/10.1016/j.ngib.2014.11.009.

IUPAC (International Union of Pure and Applied Chemistry), 1994. Physical chemistry division commission on colloid and surface chemistry, subcommittee on characterization of porous solids: recommendations for the characterization of porous solids (technical report). Pure Appl. Chem. 66 (8).

Ju, Y., Sun, Y., Tan, J., Bu, H., Han, K., Li, X., Fang, L., 2018. The composition, pore structure characterization and deformation mechanism of coal-bearing shales from tectonically altered coalfields in eastern China. Fuel 234, 626–642. https://doi.org/10.1016/j.fuel.2018.06.116.

Kassis, S., Sondergeld, C.H., 2010. Fracture permeability of gas shale: effects of roughness, fracture offset, proppant, and effective stress: society of Petroleum Engineers -. Int. Oil and Gas Confer. Exhibit. China 2010, IOGCEC 3, 1805–1821. https://doi.org/10.2523/131376-ms.

Klaver, J., Desbois, G., Littke, R., Urai, J.L., 2015. BIB-SEM characterization of pore space morphology and distribution in postmature to overmature samples from the Haynesville and Bossier Shales. Mar. Petrol. Geol. 59, 451–466. https://doi.org/10.1016/j.marpetgeo.2014.09.020.

Kwon, O., Kronenberg, A.K., Gangi, A.F., Johnson, B., 2001. Permeability of Wilcox shale and its effective pressure law. J. Geophys. Res. Solid Earth 106 (B9), 19339–19353. https://doi.org/10.1029/2001JB000273.

Kwon, O., Kronenberg, A.K., Gangi, A.F., Johnson, B., Herbert, B.E., 2004. Permeability of illite-bearing shale: 1. Anisotropy and effects of clay content and loading. J. Geophys. Res. Solid Earth 109 (10). https://doi.org/10.1029/2004JB003052.

Lai, J., Liu, B.C., Li, H. Bin, Pang, X.J., Liu, S.C., Bao, M., Wang, G.W., 2022. Bedding parallel fractures in fine-grained sedimentary rocks: recognition, formation mechanisms, and prediction using well log. Petrol. Sci. 19, 554–569. https://doi.org/10.1016/J.PETSCI.2021.10.017.

Li, S., Yuan, Y., Sun, W., Sun, D., Jin, Z., 2016. Formation and destruction mechanism as well as major controlling factors of the Silurian shale gas overpressure in the Sichuan Basin, China. J. Natural Gas Geosci. 1 (4), 287–294. https://doi.org/10.1016/J.JNGGS.2016.09.002.

Loucks, R.G., Ruppel, S.C., 2007. Mississippian Barnett shale: lithofacies and depositional setting of a deep-water shale-gas succession in the fort worth basin, Texas. AAPG (Am. Assoc. Pet. Geol.) Bull. 91 (4), 579–601.

Louis, L., Baud, P., Wong, T.F., 2009. Microstructural inhomogeneity and mechanical anisotropy associated with bedding in rothbach sandstone. Pure Appl. Geophys. 166 (5–7), 1063–1087. https://doi.org/10.1007/S00024-009-0486-1.

Ma, Y., Guo, X., Guo, T., Huang, R., Cai, X., Li, G., 2007. The Puguang gas field: new giant discovery in the mature Sichuan Basin, southwest China. AAPG (Am. Assoc. Pet. Geol.) Bull. 91 (5), 627–643. https://doi.org/10.1306/11030606062.

Ma, Y., Pan, Z., Zhong, N., Connell, L.D., Down, D.I., Lin, W., Zhang, Y., 2016. Experimental study of anisotropic gas permeability and its relationship with fracture structure of Longmaxi Shales, Sichuan Basin, China. Fuel 180, 106–115. https://doi.org/10.1016/j.fuel.2016.04.029.

Mastalerz, M., Schimmelmann, A., Drobniak, A., Chen, Y., 2013. Porosity of Devonian and Mississippian New Albany Shale across a maturation gradient: insights from organic petrology', gas adsorption, and mercury intrusion. AAPG (Am. Assoc. Pet. Geol.) Bull. 97 (10), 1621–1643. https://doi.org/10.1306/04011312194.

McKee, C.R., Bumb, A.C., Koenig, R.A., 1988. Stress-dependent permeability and porosity of coal and other geologic formations. SPE Form. Eval. 3 (1), 81–91. https://doi.org/10.2118/12858-PA.

Morgan, S.P., Einstein, H.H., 2017. Cracking processes affected by bedding planes in Opalinus shale with flaw pairs. Eng. Fract. Mech. 176, 213–234. https://doi.org/10.1016/j.engfracmech.2017.03.003.

Pang, X., Wang, G., Kuang, L., Zhao, F., Li, C., Wang, C., Zhang, M., Lai, J., 2023. Lamellation fractures in shale oil reservoirs: recognition, prediction and their influence on oil enrichment. Mar. Petrol. Geol. 148, 106032 https://doi.org/10.1016/J.MARPETGEO.2022.106032.

Ross, D.J.K., Bustin, R.M., 2007. Shale gas potential of the lower jurassic gordondale member, northeastern British columbia, Canada. Bull. Can. Petrol. Geol. 55 (1), 51–75.

Ross, D.J.K., Bustin, R.M., 2008. Characterizing the shale gas resource potential of Devonian-Mississippian strata in the Western Canada sedimentary basin: application of an integrated formation evaluation. AAPG (Am. Assoc. Pet. Geol.) Bull. 92 (1), 87–125. https://doi.org/10.1306/09040707048.

Selley, R.C., 2012. UK shale gas: the story so far. Mar. Petrol. Geol. 31 (1), 100–109. https://doi.org/10.1016/j.marpetgeo.2011.08.017.

Shi, Y., Wang, C., 1986. Pore pressure generation in sedimentary basins: overloading versus aquathermal. J. Geophys. Res. Solid Earth 91 (B2), 2153–2162.

Shi, Z., Dong, D., Wang, H., Sun, S., Wu, J., 2020. Reservoir characteristics and genetic mechanisms of gas-bearing shales with different laminae and laminae combinations: a case study of Member 1 of the Lower Silurian Longmaxi shale in Sichuan Basin, SW China. Petrol. Explor. Dev. 47 (4), 888–900. https://doi.org/10.1016/S1876-3804(20)60104-5.

Tian, H., Pan, L., Xiao, X., Wilkins, R.W.T., Meng, Z., Huang, B., 2013. A preliminary study on the pore characterization of Lower Silurian black shales in the Chuandong Thrust Fold Belt, southwestern China using low pressure N_2 adsorption and FE-SEM methods. Mar. Petrol. Geol. 48, 8–19. https://doi.org/10.1016/J.MARPETGEO.2013.07.008.

Tian, H., Zeng, L., Xu, X., Li, H., Luo, B., Dong, S., 2021. Factors influencing the in-situ stress orientations in shales: a case study of the Wufeng-Longmaxi formations in the Jiaoshiba Area, southeastern Sichuan Basin, China. J. Nat. Gas Sci. Eng. 94 https://doi.org/10.1016/j.jngse.2021.104110.

Tuo, J., Wu, C., Zhang, M., 2016. Organic matter properties and shale gas potential of Paleozoic shales in Sichuan Basin, China. J. Nat. Gas Sci. Eng. 28, 434–446. https://doi.org/10.1016/J.JNGSE.2015.12.003.

Wang, C., Zhang, B., Hu, Q., Shu, Z., Sun, M., Bao, H., 2019. Laminae characteristics and influence on shale gas reservoir quality of lower Silurian Longmaxi Formation in the Jiaoshiba area of the Sichuan Basin, China. Mar. Petrol. Geol. 109, 839–851. https://doi.org/10.1016/j.marpetgeo.2019.06.022.

Wang, Q., Lu, H., Wang, T., Liu, D., Peng, P., Zhan, X., Li, X., 2018. Pore characterization of Lower Silurian shale gas reservoirs in the Middle Yangtze region, central China. Mar. Petrol. Geol. 89, 14–26. https://doi.org/10.1016/J.MARPETGEO.2016.12.015.

Wang, X., Wang, R., Ding, W., Yin, S., Sun, Y., Zhou, X., Li, Q., 2017. Development characteristics and dominant factors of fractures and their significance for shale reservoirs: a case study from €1b2 in the Cen'gong block, southern China. J. Petrol. Sci. Eng. 159, 988–999. https://doi.org/10.1016/j.petrol.2017.08.007.

Wang, X., Jiang, Z., Jiang, S., Chang, J., Li, X., Wang, X., Zhu, L., 2020. Pore evolution and formation mechanism of organic-rich shales in the whole process of hydrocarbon generation: study of artificial and natural shale samples. Energy Fuel. 34 (1), 332–347. https://doi.org/10.1021/ACS.ENERGYFUELS.9B03789.

Wang, Y., Pu, J., Wang, L., Wang, J., Jiang, Z., Song, Y.F., Wang, C.C., Wang, Y., Jin, C., 2016. Characterization of typical 3D pore networks of Jiulaodong formation shale using nano-transmission X-ray microscopy. Fuel 170, 84–91. https://doi.org/10.1016/j.fuel.2015.11.086.

Washburn, E.W., 1921. Note on a method of determining the distribution of pore sizes in a porous material. Proc. Natl. Acad. Sci. U.S.A. 7 (4), 115–116.

Xu, X., Zeng, L., Tian, H., Ling, K., Che, S., Yu, X., Shu, Z., Dong, S., 2021. Controlling factors of lamellation fractures in marine shales: a case study of the Fuling Area in Eastern Sichuan Basin, China. J. Petrol. Sci. Eng. 207 https://doi.org/10.1016/j.petrol.2021.109091.

Yi, J., Bao, H., Zheng, A., Zhang, B., Shu, Z., Li, J., Wang, C., 2019. Main factors controlling marine shale gas enrichment and high-yield wells in South China: a case study of the Fuling shale gas field. Mar. Petrol. Geol. 103, 114–125. https://doi.org/10.1016/j.marpetgeo.2019.01.024.

Zeng, L., Lyu, W., Li, J., Zhu, L., Weng, J., Yue, F., Zu, K., 2016. Natural fractures and their influence on shale gas enrichment in Sichuan Basin, China. J. Nat. Gas Sci. Eng. 30, 1–9. https://doi.org/10.1016/J.JNGSE.2015.11.048.

Zeng, L., Shu, Z., Lyu, W., Zhang, M., Bao, H., Dong, S., Chen, S., Xu, X., 2021. Lamellation fractures in the paleogene continental shale oil reservoirs in the qianjiang depression, jianghan basin, China. Geofluids 5, 1–10. https://doi.org/10.1155/2021/6653299.

Zeng, W., Zhang, J., Ding, W., Zhao, S., Zhang, Y., Liu, Z., Jiu, K., 2013. Fracture development in Paleozoic shale of Chongqing area (South China). Part one: fracture characteristics and comparative analysis of main controlling factors. J. Asian Earth Sci. 75, 251–266. https://doi.org/10.1016/j.jseaes.2013.07.014.

Zhang, L., Lu, S., Jiang, S., Xiao, D., Chen, L., Liu, Y., Zhang, Y., Li, B., Gong, C., 2018. Effect of shale lithofacies on pore structure of the wufeng-longmaxi shale in southeast chongqing, China. Energy Fuel. 32 (6), 6603–6618. https://doi.org/10.1021/ACS.ENERGYFUELS.8B00799.

Zhang, X., Shi, W., Hu, Q., Zhai, G., Wang, R., Xu, X., Meng, F., Liu, Y., Bai, L., 2020. Developmental characteristics and controlling factors of natural fractures in the lower paleozoic marine shales of the upper Yangtze Platform, southern China. J. Nat. Gas Sci. Eng. 76 https://doi.org/10.1016/j.jngse.2020.103191.

Zhang, X., Shi, W., Hu, Q., Zhai, G., Wang, R., Xu, X., Xu, Z., Meng, F., Liu, Y., 2019. Pressure–dependent fracture permeability of marine shales in the Northeast Yunnan area. Southern China: Int. J. Coal Geol. 214, 103237 https://doi.org/10.1016/j.coal.2019.103237.

Zhang, Y., He, Z., Jiang, S., Lu, S., Xiao, D., Chen, G., Li, Y., 2019. Fracture types in the lower Cambrian shale and their effect on shale gas accumulation, Upper Yangtze. Mar. Petrol. Geol. 99, 282–291. https://doi.org/10.1016/J.MARPETGEO.2018.10.030.

Zhao, W., Li, J., Yang, T., Wang, S., Huang, J., 2016. Geological difference and its significance of marine shale gases in South China. Petrol. Explor. Dev. 43 (4), 547–559. https://doi.org/10.1016/S1876-3804(16)30065-9.